Thermoelectric and Magnetic Properties of $Pr_{1-x}Sr_xMnO_3$ ($0.1 \leqq x \leqq 0.7$)

Hiroshi Nakatsugawa[1,*1], Masaki Kubota[1,*2] and Miwa Saito[2]

[1]*Graduate School of Engineering, Yokohama National University, Yokohama 240-8501, Japan*
[2]*Department of Materials and Life Chemistry, Faculty of Engineering, Kanagawa University, Yokohama 221-8686, Japan*

In this study, polycrystalline samples of $Pr_{1-x}Sr_xMnO_3$ ($0.1 \leqq x \leqq 0.7$) were synthesized using a conventional solid-state reaction method. We investigated crystal structure, magnetic susceptibility (χ), and thermoelectric properties, such as electrical resistivity (ρ), Seebeck coefficient (S), and thermal conductivity (κ), as a function of temperature (T) or Sr content (x). The crystal structure at room temperature changed from orthorhombic *Pbnm* phases, with $x \leqq 0.4$, to tetragonal *I4/mcm* phases, with $x \geqq 0.5$. The samples for $x \leqq 0.5$ showed the ferromagnetic-like ground state below Curie temperature. Conversely, the samples for $x = 0.5$, 0.6, and 0.7 showed the charge-ordering ground state below 160 K, the A-type antiferromagnetic ground state below 310 K, and the C-type antiferromagnetic ground state below 318 K, respectively. Above room temperature, all the samples exhibited adiabatic small polaron conduction in a competition between the double exchange interaction and the Jahn-Teller distortion. Although the samples for $x = 0.1$ and 0.2 showed a large positive S below room temperature, the carrier type changed from hole-like to electron-like behavior above 1000 K and 500 K, respectively. Thus, all the samples for $0.1 \leqq x \leqq 0.7$ showed a negative S at a high temperature. The largest dimensionless figure of merit (ZT) of all the samples above room temperature was 0.085 at 1073 K for $x = 0.7$, by a decrease in both ρ and lattice κ, and an increase in S. In addition, we obtained the largest ZT in the p-type specimens for $x = 0.1$, thus, attaining a maximum value of 0.0035 at 468 K. We discuss this behavior in terms of the potentiality to fabricate the oxide thermoelectric modules consisting of the same type of elements. [doi:10.2320/matertrans.E-M2015807]

1. Introduction

Thermoelectric energy conversion technology attracts renewed interest as a new energy resource.[1] Thermoelectric materials can directly convert waste heat from automobiles, facilities, and power plants into electrical energy. Since electrons in solids carry electricity together with thermal entropy, there is a finite coupling between the electrical and heat currents, which is known as the thermoelectric phenomena. The potentiality of thermoelectric materials is indicated in terms of the dimensionless figure of merit, i.e., $ZT = S^2\sigma T/\kappa$, where S, σ, κ, and T are the Seebeck coefficient, the electric conductivity, the thermal conductivity, and the absolute temperature, respectively. In addition, the thermoelectric energy conversion generates energy from the temperature gradient and the heat flow. The thermoelectric energy conversion efficiency η is defined by the ratio between the output electrical power P with the heat flux Q, i.e., $\eta = P/Q$. By optimizing the efficiency with respect to load resistance, the maximum efficiency η_{max} is obtained as a monotonically increasing function of ZT and increases with increasing a temperature difference at a high temperature. In this respect, therefore, oxides are quite attractive because they are thermally and chemically stable for long time use at high temperatures in air for thermoelectric conversion.

Recently, oxides have been studied extensively as a possible candidate for thermoelectric materials at high temperatures (above 1000 K) since the discovery of large Seebeck coefficient ($S = 100\,\mu V/K$) and low electric resistivity ($\rho = 20\,m\Omega m$) at room temperature in the layered cobalt oxide Na_xCoO_2.[2] Furthermore, the misfit-layered cobalt oxide $Ca_3Co_4O_9$ has been studied as a candidate for p-type thermoelectric materials and typically exhibits $S = $

130 $\mu V/K$, $\rho = 150\,m\Omega m$, and $\kappa = 1.0\,W/mK$ at room temperature.[3] For instance, fabrication of power generation using oxide thermoelectric module consisting of p-type $Ca_{2.7}Bi_{0.3}Co_4O_9$ and n-type $La_{0.9}Bi_{0.1}NiO_3$ bulks have been reported.[4] In fact, power charging a portable phone has been successful using this oxide thermoelectric module though the maximum efficiency η_{max} was as low as 1.4%.[5] To enhance η_{max}, Urata *et al.*[6] have built thermoelectric modules consisting of p-type $Ca_{2.7}Bi_{0.3}Co_4O_9$ and n-type $CaMn_{0.98}$-$Mo_{0.02}O_3$ bulks and calculated η_{max} to be 2.0% from ZT values. However, the n-type elements were damaged by thermal stress between the alumina substrate and the element.[6] To overcome such a lack of oxide thermoelectric materials, we have paid attention to perovskite-type oxides which can form both n-type and p-type conductors with the general formula ABO_3.

Perovskite-type oxides such as titanate,[7] manganate,[8] ferrate,[9] and cobaltate[10] phases reveal a large Seebeck coefficient, S, which is one of the essential prerequisites for potential thermoelectric materials. The large S values are caused by a strong interplay between charges, orbital, spin states, and crystal structure. Koshibae *et al.*[11] proposed that the high-temperature limit of S values in 3d transition metal oxides is given by Heikes formula from a localized picture. When a degeneracy of spin and orbital degrees of freedom in 3d transition metal ions gives large value, the large S can be expected. Therefore, control of spin and orbital states of 3d transition metal ions would improve the ZT values of thermoelectric oxides. In this sense, electron-doped manganates showed promising n-type thermoelectric properties at high-temperatures,[8,12–18] although perovskite-type Mn oxides have been already widely studied due to their colossal magnetoresistance (CMR) at low-temperature,[19,20] which was explained by a competition between the double exchange (DE) interaction[21] and the Jahn-Teller (JT) distortion of MnO_6 octahedra.[22] For polycrystalline n-type $Ca_{0.9}Yb_{0.1}$-

*1Corresponding author, E-mail: naka@ynu.ac.jp
*2Graduate Student, Yokohama National University

MnO_3, D. Flahaut et al.[17] reported the ZT value of 0.16 at 1000 K in air. However, there is remarkably little known about the p-type thermoelectric properties in manganates. In the present study, we prepared polycrystalline samples of $Pr_{1-x}Sr_xMnO_3$ ($0.1 \leqq x \leqq 0.7$), and investigate p- and n-type thermoelectric properties by taking account of the effect of Sr-doping on both crystal structures and magnetic properties in order to clarify the ZT values of the materials.

2. Experimental Procedure

Polycrystalline samples of $Pr_{1-x}Sr_xMnO_3$ ($0.1 \leqq x \leqq 0.7$) were synthesized by a conventional solid-state reaction method. The compounds starting from stoichiometric mixtures of Pr_6O_{11} (99.9%, Wako Pure Chemical Industries, Ltd.), $SrCO_3$ (99.99%, Wako Pure Chemical Industries, Ltd.), and Mn_2O_3 (99.9%, Kojundo Chemical Laboratory Co., Ltd.) in an agate mortar with ethanol were calcinated at 1373 K for 24 h in air. The calcined powders were pressed into pellets under a pressure of 16 MPa and sintered in pure flowing nitrogen gas at 1673 K for 48 h. The pellets were cooled down to room temperature in the furnace. Powder X-ray diffraction (XRD) data were collected with a diffractometer (RINT2500, Rigaku Co.) using CuKα ($\lambda = 1.542$ Å) radiation with a pyrolytic graphite monochromator at room temperature. Crystal structure parameters were refined by the Rietveld analysis using the RIETAN-FP program[23] with XRD data in 2θ range from 10° to 90° with a scan step of 0.02°.

The resistivity ρ was measured by a van der Pauw technique in the temperature range from 80 to 395 K using a commercial apparatus (ResiTest8300, TOYO Co.) and by the direct-current four-probe method in the temperature range from 373 to 1073 K using a ZEM-3 apparatus (ULVAC-RIKO Co.). The Seebeck coefficient S was measured using a steady-state technique in the temperature range from 80 to 395 K by the ResiTest8300 apparatus (TOYO Co.) and in the temperature range from 373 to 1073 K by the ZEM-3 apparatus (ULVAC-RIKO Co.). S was determined by the least-squares approximation from a plot of the thermal electromotive force against the temperature difference, where the contribution of lead wires was subtracted. The Hall coefficient R_H at room temperature was measured using the ResiTest8300 apparatus (TOYO Co.) under a magnetic field of 0.85 T using the van der Pauw technique. In the evaluation of carrier concentration n, the Hall scattering factor was assumed to obey a single carrier model. Thus, n was calculated from $1/e|R_H|$, where e is the elementary electric charge, and the Hall mobility μ was also calculated from $|R_H|/\rho$.

The thermal conductivity κ was calculated from the thermal diffusivity α, the specific heat at constant volume C_V, and the bulk density d using the relationship: $\kappa = d\alpha C_V$. The bulk density was measured by the Archimedes method at room temperature using a specific gravity measurement kit (SMK-401, SHIMADZU Co.). The relative density for all the samples was measured in the range about 90–95%. The specific heat was determined by differential scanning calorimetry (DSC) using in the temperature range from 303 to 323 K using an X-DSC7000 apparatus (Hitachi High-Tech
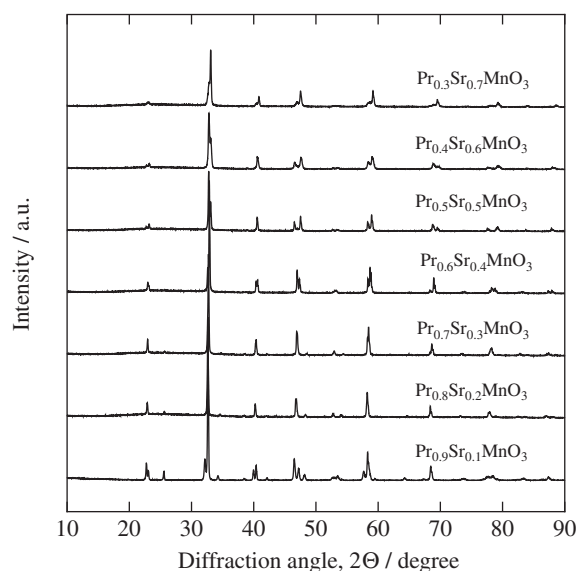

Fig. 1   X-ray diffraction patterns of $Pr_{1-x}Sr_xMnO_3$ ($0.1 \leqq x \leqq 0.7$) at room temperature.

Science Co.). The specific heat for all the samples was measured in the range 300–700 J/(kg K). In addition, the thermal diffusivity was measured in air from 573 to 1073 K with step of 100 K, using a laser flash method (TC-7000, ULVAC-RIKO Co.). This apparatus uses both a solid-state laser ($\lambda = 1.06$ µm) to heat one side of the polycrystalline sample and an InSb infrared detector to measure the corresponding heat increase on the back side. The method is based on the laser flash technique invented by Parker et al.[24]

The magnetic susceptibility χ was measured in the temperature range 5 K to room temperature using a superconducting quantum interference device (SQUID) magnetometer (MPMS, Quantum Design, Inc.) under zero-field cooling (ZFC) condition at a magnetic field of 0.1 T or 1 T in a warming process.

3. Results and Discussion

The XRD data confirm that all samples are the single phase with an orthorhombic perovskite structure of $Pbnm$ space group for $x \leqq 0.4$ and with a tetragonal perovskite structure of $I4/mcm$ space group for $x \geqq 0.5$ (see Fig. 1). Tokura et al.[25] reported that the three-dimensional (3D) ferromagnetic (FM) metallic ground state shows up for $x \geqq 0.3$, yet the insulating charge ordering (CO) ground state sets in below the CO temperature for $x = 0.5$. On the other hand, the ground states of samples for $x > 0.5$ are both the A-type antiferromagnetic (AFM) ground state for $x \sim 0.55$–0.57 with the metallic two-dimensional (2D) FM coupling in the MnO_2 layers and the C-type AFM insulating ground state for $x > 0.6$ with polaronic conductivity along the one-dimensional (1D) FM coupling, i.e., MnO chains.[26–28] Furthermore, above room temperature, the crystal structure changes from orthorhombic $Pbnm$ phases with $x \leqq 0.4$ to orthorhombic $Ibmm$ phases with $0.4 < x < 0.5$ and tetragonal $I4/mcm$ phases with $x \geqq 0.5$.[26–28] Our results are consistent with prior studies,[26–28] as shown in Fig. 1 and Table 1.

Table 1   Crystal structure parameters of $Pr_{1-x}Sr_xMnO_3$ ($0.1 \leqq x \leqq 0.7$) at room temperature.

composition, x		0.1	0.2	0.3	0.4	0.5	0.6	0.7
space group		*Pbnm*	*Pbnm*	*Pbnm*	*Pbnm*	*I4/mcm*	*I4/mcm*	*I4/mcm*
Goldschmidt tolerance factor		0.885	0.895	0.905	0.915	0.925	0.935	0.945
orthorhombicity factor: b/a		1.0155	1.0024	0.9955	0.9918	1.0000	1.0000	1.0000
a (Å)		5.4692(4)	5.4781(3)	5.4797(2)	5.4828(2)	5.3978(4)	5.3874(6)	5.3846(5)
b (Å)		5.5541(4)	5.4914(3)	5.4550(2)	5.4377(2)	5.3978(4)	5.3874(6)	5.3846(5)
c (Å)		7.6872(5)	7.7336(4)	7.7113(3)	7.6648(3)	7.7816(5)	7.7670(9)	7.618(1)
V (Å³)		233.51(3)	232.64(2)	230.50(1)	228.52(1)	226.72(2)	225.43(4)	220.89(5)
Pr/Sr	x	−0.007(0)	−0.006(0)	−0.002(0)	−0.003(0)	0.000	0.000	0.000
	y	0.039(0)	0.030(0)	0.019(0)	0.000(0)	0.500	0.500	0.500
	z	0.250	0.250	0.250	0.250	0.250	0.250	0.250
	B (Å²)	0.500	0.500	0.500	0.500	0.500	0.500	0.500
	g	1.000	1.000	1.000	1.000	1.000	1.000	1.000
Mn	x	0.500	0.500	0.500	0.500	0.000	0.000	0.000
	y	0.000	0.000	0.000	0.000	0.000	0.000	0.000
	z	0.000	0.000	0.000	0.000	0.000	0.000	0.000
	B (Å²)	0.500	0.500	0.500	0.500	0.500	0.500	0.500
	g	1.000	1.000	1.000	1.000	1.000	1.000	1.000
O1	x	0.073(1)	0.057(3)	0.063(2)	0.046(2)	0.000	0.000	0.000
	y	0.494(1)	0.492(2)	0.501(2)	0.455(3)	0.000	0.000	0.000
	z	0.250	0.250	0.250	0.250	0.250	0.250	0.250
	B (Å²)	1.000	1.000	1.000	1.000	1.000	1.000	1.000
	g	1.000	1.000	1.000	1.000	1.000	1.000	1.000
O2	x	0.718(1)	0.731(3)	0.718(2)	0.775(2)	0.777(1)	0.774(1)	0.770(3)
	y	0.291(1)	0.298(2)	0.277(2)	0.255(3)	0.277(1)	0.274(1)	0.270(3)
	z	0.034(0)	0.035(1)	0.034(1)	0.023(1)	0.000	0.000	0.000
	B (Å²)	1.000	1.000	1.000	1.000	1.000	1.000	1.000
	g	1.000	1.000	1.000	1.000	1.000	1.000	1.000
R_{wp} (%)		11.841	6.851	6.778	7.377	9.268	9.218	14.268
R_P (%)		8.812	5.300	5.075	5.756	6.996	6.920	10.373
R_R (%)		12.004	19.290	15.183	16.836	22.200	16.962	31.514
R_ε (%)		5.367	4.443	4.572	4.480	4.976	5.157	4.884
R_B (%)		2.768	5.247	3.925	3.657	4.374	1.982	3.120
R_F (%)		1.871	6.238	5.019	5.817	4.355	1.703	2.478
Mn-O1 (Å)	×2	1.964(2)	1.959(3)	1.959(2)	1.948(2)	1.9454(1)	1.9418(2)	1.9046(4)
Mn-O2 (Å)	×2	1.942(8)	1.86(1)	1.94(1)	1.81(1)	1.919(1)	1.914(1)	1.910(2)
Mn-O2 (Å)	×2	2.032(8)	2.09(1)	1.97(1)	2.06(1)	1.919(1)	1.914(1)	1.910(2)
Mn-O1-Mn (deg.)		156.1(6)	161(1)	159.4(8)	159.2(8)	180.0	180.0	180.0
Mn-O2-Mn (deg.)		157.3(3)	157.8(6)	159.4(5)	168.3(7)	167.4(6)	168.6(5)	170(1)

The structural parameters were determined by Rietveld refinement method by using the profile analysis program RIETAN-FP[23] (see Table 1). In this work, the isotropic atomic displacement parameters B in the analysis were fixed, both of Pr/Sr sites and Mn sites were 0.5, and both of apical oxygen (O1) sites and equatorial oxygen (O2) sites were 1.0, respectively. A split pseudo-Voigt function was used to fit the Bragg peak shapes. The weighted profile reliability factors of the Rietveld refinement R_{wp} were in the range from about 7 to 14%. This means there is good fitting between observed and calculated intensities. It can be seen that lattice parameters a, b, and c and unit cell volume $V = abc$ decrease with increasing Sr content x. This is mostly because substituting Sr^{2+} for Pr^{3+} introduces Mn^{4+} sites in the Mn^{3+} matrix, whereas the ionic radius of Mn^{4+} ion in the high-spin (HS) state is much smaller than that of Mn^{3+} ion in the HS state, i.e., 0.530 Å for Mn^{4+} and 0.645 Å for Mn^{3+}, respectively.[29]

The orthorhombic distortions, characterized by the Mn-O1 and Mn-O2 distances and the distortion angles (Mn-O1-Mn and Mn-O2-Mn), are also listed in Table 1 along with the Goldschmidt tolerance factor[30] and the orthorhombicity factor. The Goldschmidt tolerance factor for the perovskite structure ABO_3 is defined by $(r_A + r_O)/\sqrt{2}(r_B + r_O)$ and represents a structural parameter describing geometric distortion. For $0.1 \leqq x \leqq 0.4$, an increase in the tolerance factor with increasing x was observed, indicating that the MnO_6 octahedral distortion is suppressed with increasing x. This distortion is also confirmed by the simultaneous decrease of the orthorhombicity factor and the fact that the crystal structure changes from the orthorhombic *Pbnm* phases to the tetragonal *I4/mcm* phases.

Figure 2 shows the temperature variation of dc-susceptibility χ under a magnetic field of 0.1 T or 1 T for $0.1 \leqq x \leqq 0.7$, measured in the warming process up to room
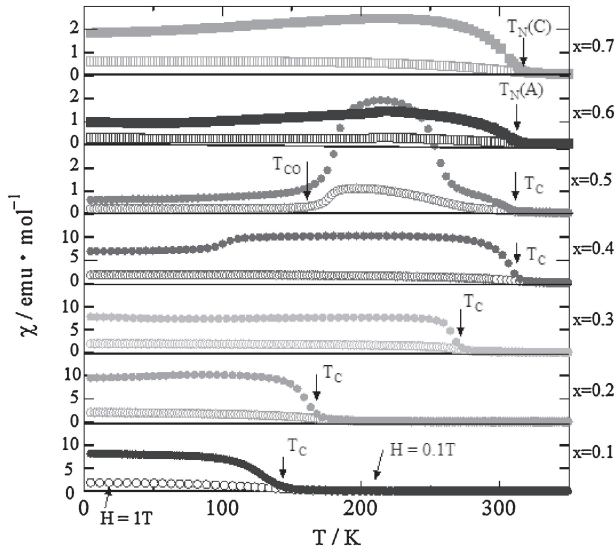
Fig. 2 Temperature (T) dependence of magnetic dc-susceptibility (χ) for Pr$_{1-x}$Sr$_x$MnO$_3$ (0.1 $\leq$ x $\leq$ 0.7) under zero-field cooling condition at a magnetic field of 01 T (solid circles and squares) or 1 T (open circles and squares) in a warming process. Arrows show the magnetic transition temperatures.
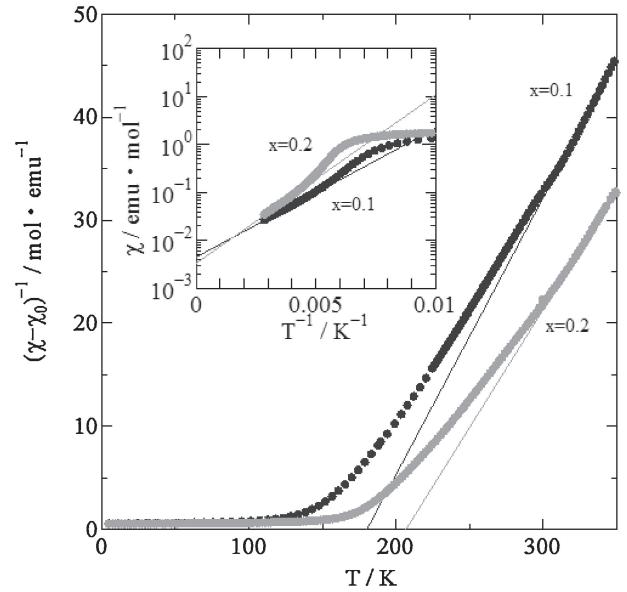

Fig. 3 Temperature (T) dependence of inverse magnetic susceptibility $1/(\chi - \chi_0)$ for $x = 0.1$ and 0.2, where the straight lines represent the Curie-Weiss laws. The inset shows magnetic susceptibility (χ) as a function of $1/T$ for $x = 0.1$ and 0.2, where temperature-independent term (χ_0) is evaluated from $\chi(T \to \infty)$.

Table 2 Temperature-independent magnetic susceptibilities (χ_0), paramagnetic Curie temperatures (Θ), Curie constants (C), effective magnetic moments (μ_{eff}), and valence state of Mn ions for Pr$_{0.9}$Sr$_{0.1}$MnO$_3$ ($x = 0.1$) and Pr$_{0.8}$Sr$_{0.2}$MnO$_3$ ($x = 0.2$).

composition, x	0.1	0.2
χ_0 (emu/mol)	0.004	0.003
Θ (K)	190	238
C (emu K/mol)	3.58	3.31
μ_{eff} (μ_B)	5.35	5.14
valence state of Mn ion	2.6	2.8

temperature after ZFC down to 5 K. The temperature dependence of χ suggests that the data of all samples under a magnetic field of 1 T are suppressed rather than under a magnetic field of 0.1 T. This implies that both ferromagnetism and antiferromagnetism coexists in all samples. The samples have a Curie temperature T_C of 145, 168, 271, 310, and 310 K for x = 0.1, 0.2, 0.3, 0.4, and 0.5, respectively. In particular, the samples for x = 0.2, 0.3 and 0.4 have a clear FM ground state below T$_C$ while the sample for x = 0.5 has an additional transition below 160 K which is attributed to the charge ordering (CO) ground state[25] arising due to a competition between the MnO$_6$ octahedral distortion (tolerance factor is 0.900) and the nominal concentration of x = 0.5. In addition, the ground state of x = 0.1 sample is the spin-canted insulating state below 100 K.[25] For x = 0.5, the ferromagnetism exists at intermediate temperature between 160 and 310 K. For x > 0.5, the ferromagnetism disappears almost entirely and the ground state for x = 0.6 and 0.7 is the A-type AFM with 2D FM coupling in MnO$_2$ layers below $T_N(A)$ = 310 K and the C-type AFM with 1D FM coupling along MnO chains below $T_N(C)$ = 318 K.[26]

Figure 3 shows the plots of the inverse dc-susceptibility $(\chi - \chi_0)^{-1}$ for the specimens of x = 0.1 and 0.2 versus temperature T, where χ_0 is the contribution of temperature-independent magnetic susceptibility. The curves are strictly linear in the high-temperature paramagnetic (PM) range. As shown in Fig. 3, the PM properties are best manifested by the plot of reciprocal susceptibilities. The PM properties can be expressed as: $\chi = \chi_0 + C/(T - \Theta)$, where C is the Curie constant and Θ is the paramagnetic Curie temperature. The effective magnetic moment of each Mn site μ_{eff} is then determined using the obtained C in the equation

$$\mu_{\text{eff}} = 2\sqrt{S(S+1)}\mu_B = \sqrt{\frac{3k_B C}{N_A}}, \qquad (1)$$

where k_B, μ_B, N_A, and S are the Boltzmann constant, the Bohr magnetron, the Avogadro's number, and the spin quantum

number, respectively. Since the Mn^{3+}($t_{2g}^3 e_g^1$) and Mn^{4+}(t_{2g}^3) ions in the perovskite-type Mn oxides are in the HS state, the valence state of each Mn ion can be directly derived from eq. (1). Table 2 summarizes the Temperature-independent magnetic susceptibilities, paramagnetic Curie temperatures, Curie constants, effective magnetic moments, and valence state of Mn ions for Pr$_{0.9}$Sr$_{0.1}$MnO$_3$ and Pr$_{0.8}$Sr$_{0.2}$MnO$_3$. The nominal valence state of Mn ions for both specimens is 3.1 for x = 0.1 and 3.2 for x = 0.2, respectively. From the C, however, the valence state of Mn ions is 2.6 for x = 0.1 and 2.8 for x = 0.2, respectively. This discrepancy is eliminated by measuring dc-susceptibility above 350 K.

Temperature dependence of the electrical resistivity ρ for the specimens of 0.1 $\leq$ x $\leq$ 0.7 measured in the temperature range from 80 to 1073 K are summarized in Fig. 4. The samples for x = 0.1 and 0.2 show a semiconducting behavior over the whole temperature range. In particular, the samples have the T_C of 168, 271, 310, and 310 K for x = 0.2, 0.3, 0.4, and 0.5, respectively. Besides, x = 0.3 and 0.4 have a clear metal-insulator (M-I) transition due to a competition between the DE interaction[21] and the JT distortion of MnO$_6$ octahedra.[22] at 271 K and 310 K, respectively. For x = 0.2,
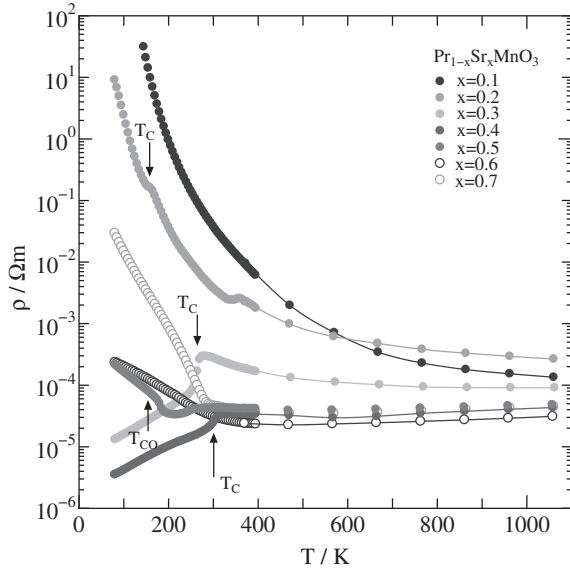
Fig. 4   Temperature (T) dependence of electric resistivity (ρ) for $Pr_{1-x}Sr_x$-MnO_3 ($0.1 \leqq x \leqq 0.7$), where arrows show the magnetic transition temperatures of $x = 0.2$, 0.3, 0.4, and 0.5.

Fig. 5   Arrhenius relations between σT and $1/T$ for $Pr_{1-x}Sr_xMnO_3$ ($0.1 \leqq x \leqq 0.7$) above 100 K, where arrows show the magnetic transition temperatures of $x = 0.2$, 0.3, 0.4, and 0.5. The straight lines represent linear portions in the Arrhenius plots.

on the other hand, there is no transition into a metallic state despite the FM ground state below 168 K because of a competition between the DE interaction and the super-exchange interaction which favors an AFM spin state, rendering both a canted magnetic structure and an insulating ground state.[31] Also for the specimens of $x \geqq 0.5$ the insulating ground states, i.e., CO ground state[25] for $x = 0.5$ below $T_{CO} = 160$ K, the A-type AFM with 2D FM coupling in MnO_2 layers[26] for $x = 0.6$ below $T_N(A) = 310$ K, and the C-type AFM with 1D FM coupling along MnO chains[26] for $x = 0.7$ below $T_N(C) = 318$ K are obtained, respectively.

All samples exhibited an adiabatic small polaron behavior in the conduction mechanism above room temperature. For small polaron hopping conduction, in which the carrier mobility μ obeys thermally activated temperature depend-ence, rather than the carrier concentration n, with the activation energy, i.e., the small polaron binding energy. Therefore, the temperature dependence of the electrical conductivity σ predicted using the polaron theory is as follows:[32–34]

$$\sigma = en\mu$$
$$= en_0 \frac{e\omega_{LO}a^2}{k_BT} \exp\left(-\frac{W_H + E_g/2}{k_BT}\right),$$
$$= \frac{\sigma_0}{T} \exp\left(-\frac{E_\sigma}{k_BT}\right) \qquad (2)$$

where $n = n_0 \exp(-E_g/2k_BT)$ denotes the number of hopping small polarons per unit volume, n_0 is the concen-tration of Mn^{4+} sites per unit volume, ω_{LO} is the optical-phonon frequency, a is the characteristic intersite hopping distance that corresponds to a typical Mn-O-Mn distance of our samples, W_H is the hopping energy of small polarons, σ_0 is the pre-exponential term, and E_σ is the activation energy of the conduction process. As is clearly shown in Fig. 5, all the electrical conductivities above room temperature are well described by the activated conduction process. The Arrhenius relation of σT against $1/T$ above room temperature plotted in
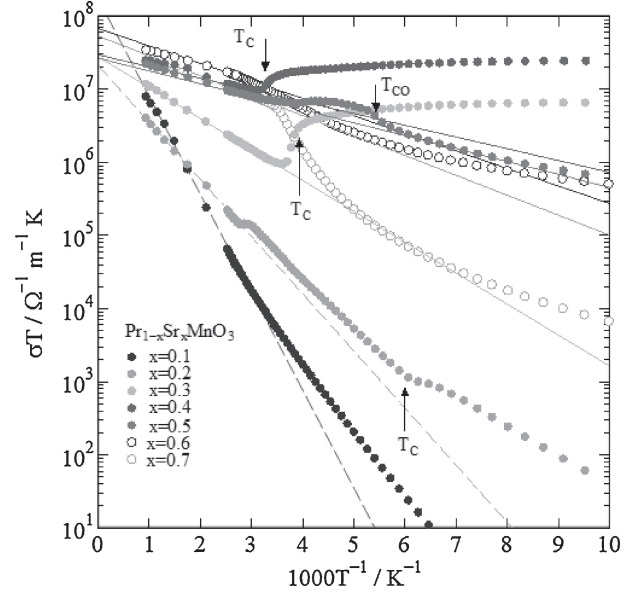
Fig. 5 yield well straight lines with E_σ of 0.27, 0.16, 0.08, 0.03, 0.04, 0.05, and 0.05 eV for $x = 0.1$, 0.2, 0.3, 0.4, 0.5, 0.6, and 0.7, respectively. Furthermore, as listed in Table 3, the least mean square fitting yields σ_0 in the range 10^7–$10^8 \Omega^{-1} m^{-1}$ K by extrapolating σT at $1/T \to 0$ in Fig. 5. Employing $\omega_{LO} \approx 10$ *THz*, $a \approx 4.0$ Å which is the mean Mn-O-Mn distance determined by Rietveld refinement method listed in Table1, and $n_0 \approx 10^{27}$–$10^{28} m^{-3}$ calculated from lattice parameters in Table 1, σ_0 is also calculated to be in the range 10^6–$10^7 \Omega^{-1} m^{-1}$ K as summarized in Table 3. Taking into account of the effect of polycrystallinity in samples and the uncertainty in the value employed for ω_{LO}, the agree-ments are good.

Figure 6 shows the temperature dependence of the Seebeck coefficient S for the specimens of $0.1 \leqq x \leqq 0.7$ measured in the temperature range up to 1073 K. The sample for $x = 0.1$ shows a large positive S below room temperature and a sharp fall above room temperature. The positive S for $x = 0.2$ decreases gradually below T_C. The samples for $x = 0.3$ and 0.4 show a small positive S below T_C and a negative S above T_C. The samples for $x = 0.5$ and 0.6 show a negative S over the whole temperature range. For high-temperature extrapolation, we assumed the expression for the temperature dependence of S above room temperature with T^{-1} dependence according to the following equation

$$S = S_\infty + \frac{k_B}{e}\frac{E_S}{k_BT}, \qquad (3)$$

where $E_S(E_\sigma \gg E_S)$ is a characteristic energy for S, and S_∞ is a temperature independent term, i.e., the thermopower in the high-temperature limit.[31] Table 3 lists the experimental values of E_S and S_∞ for the specimens of $0.1 \leqq x \leqq 0.7$ obtained from these least-mean-square fits. If we assume that the values of E_S correspond to $E_g/2$ in eq. (2), the hopping energy can be expressed as $W_H = E_\sigma - E_S$. The values of W_H for $0.1 \leqq x \leqq 0.7$ are also listed in Table 3.

Table 3 Magnetic transition temperatures (T_C and T_N), activation energy of electric conduction (E_σ), experimental pre-exponential term (σ_0), calculated pre-exponential term (σ_0), hopping energy of small polarons (W_H), characteristic energy of Seebeck coefficient (E_S), concentration of Mn^{4+} sites per unit volume (n_0), Seebeck coefficient in the high-temperature limit (S_∞), S_∞ evaluated to be $-k_B \ln[10/4 \cdot x/(1-x)]/e$, i.e., S_A, S_∞ evaluated to be $-k_B \ln[5/4 \cdot x/(1-x)]/e$, i.e., S_B, X in the relation of $S_A(1-X) + S_B X$, absolute value of Hall coefficient at room temperature ($|R_H|$), experimental error of $|R_H|$ at room temperature, carrier concentration at room temperature (n), Hall mobility at room temperature (μ), bulk density at room temperature (d), relative density at room temperature, and specific heat at room temperature (C_V) for Pr$_{1-x}$Sr$_x$MnO$_3$ (0.1 ≦ x ≦ 0.7).

composition, x	0.1	0.2	0.3	0.4	0.5	0.6	0.7
T_C (K), T_N (K)*	145	168	271	313	313	313*	318*
E_σ (eV)	0.266	0.155	0.084	0.032	0.035	0.048	0.054
experimental σ_0 (Ω^{-1} m^{-1} K)	1.68×10^4	2.12×10^3	2.78×10^3	2.95×10^3	2.67×10^3	6.81×10^3	5.35×10^3
calculated σ_0 (Ω^{-1} m^{-1} K)	4.61×10^2	9.10×10^2	1.37×10^3	1.85×10^3	2.20×10^3	2.64×10^3	3.11×10^3
W_H (eV)	0.219	0.135	0.079	0.028	0.030	0.040	0.040
E_S (eV)	0.047	0.020	0.005	0.004	0.005	0.008	0.014
concentration of Mn^{4+}, n_0 (m^{-3})	1.58×10^{27}	3.15×10^{27}	4.80×10^{27}	6.62×10^{27}	7.98×10^{27}	9.59×10^{27}	1.15×10^{28}
S_∞ (μV/K)	−51.1	−35.1	−25.8	−31.7	−40.5	−55.8	−82.2
S_A (μV/K)	110.4	40.5	−5.9	−44.0	−79.0	−113.9	−152.0
S_B (μV/K)	170.1	100.2	53.8	15.7	−19.2	−54.2	−92.2
X in $S_A(1-X) + S_B X$	0	0	0	0.206	0.644	0.973	1
$|R_H|$ (μm^3/C) @RT	0.9(2)	0.4(1)	0.0070(6)	0.0086(4)	0.0037(8)	0.008(2)	0.003(1)
Experimental error of $|R_H|$ @RT (%)	21	19	10	5	23	35	27
n (m^{-3}) @RT	$6(1) \times 10^{24}$	$1.6(6) \times 10^{25}$	$9(1) \times 10^{26}$	$7.2(3) \times 10^{26}$	$1.7(3) \times 10^{27}$	$9(3) \times 10^{26}$	$1.7(5) \times 10^{27}$
μ ($\times 10^{-4}$ m^2/Vs) @RT	0.25(5)	0.6(2)	0.25(2)	3.5(1)	0.8(2)	2.5(9)	0.7(2)
d (kg/m^3) @RT	6260	6106	6049	6119	5749	5596	5662
Relative density (%)	92.3	91.7	92.1	94.6	90.4	90.1	90.5
C_V (J/kg K) @RT	700	600	400	500	400	500	300

Koshibae *et al.*[11] have proposed that S_∞ of the 3d transition-metal oxides is described by an extended Heikes formula.[35] According to their theoretical predictions, S_∞ of Pr$_{1-x}$Sr$_x$MnO$_3$ is expressed as

$$S_\infty = -\frac{k_B}{e} \ln\left(\frac{g_{Mn^{3+}}}{g_{Mn^{4+}}} \frac{x}{1-x}\right), \qquad (4)$$

where x is the concentration of Mn^{4+} ions, and the ratio $g_{Mn^{3+}}/g_{Mn^{4+}}$ means an unbalance of the degeneracy of the spin and the orbital degrees of freedom between Mn^{3+} and Mn^{4+}. Since Mn^{3+} and Mn^{4+} ions are in the high spin state, $g_{Mn^{4+}}$ is equal to 4 owing only to the spin degeneracy of t_{2g}^3 and $g_{Mn^{3+}}$ is equal to 10 owing to both the spin and orbital degeneracy of $t_{2g}^3 e_g^1$. As listed in Table 3, S_∞ is evaluated to be

$$S_\infty = S_A = -79.0 \, \mu\text{V/K} - \frac{k_B}{e} \ln\frac{x}{1-x}. \qquad (5)$$

However, S_A is not in good agreement with the experimental values of S_∞. The samples for $x = 0.1$ and 0.2 are evaluated a positive S_A, whereas, negative S_∞ is obtained by extrapolating S at $1/T \to 0$ in Fig. 6. We do not have a clear answer for this yet, but suggest a possible scenario that the thermopower for $x = 0.1$ and 0.2 changes sign from apparent holelike to electronlike behavior above 1000 K and 500 K, respectively. The samples for $x > 0.3$ are evaluated S_A to be $-44.0 \, \mu\text{V/K}$ for $x = 0.4$, $-79.0 \, \mu\text{V/K}$ for $x = 0.5$, -113.9 μV/K for $x = 0.6$, and $-152.0 \, \mu\text{V/K}$ for $x = 0.7$, respectively. By contrast, the experimental values of S_∞ are -31.7 μV/K for $x = 0.4$, $-40.5 \, \mu\text{V/K}$ for $x = 0.5$, $-55.8 \, \mu\text{V/K}$ for $x = 0.6$, and $-82.2 \, \mu\text{V/K}$ for $x = 0.7$, respectively. Since the
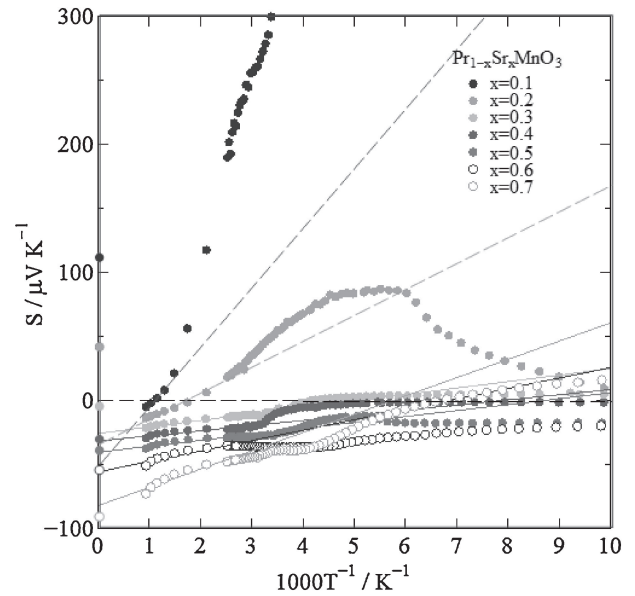

Fig. 6 Temperature (T) dependence of Seebeck coefficient (S) for Pr$_{1-x}$Sr$_x$MnO$_3$ (0.1 ≦ x ≦ 0.7) above 100 K, where the straight lines represent the theoretical relation of eq. (3). The plots at $T \to \infty$ represent $S_A(1 - X) + S_B X$, where $X = 0, 0, 0, 0.206, 0.644, 0.973$, and 1 for $x = 0.1, 0.2, 0.3, 0.4, 0.5, 0.6$, and 0.7, respectively.

JT distortion is gradually effective for the polaron formation in the samples for $x > 0.3$, the e_g level splitting is valid (no orbital degeneracy in Mn^{3+}), and $g_{Mn^{3+}}$ is equal to 5 owing only to the spin degeneracy of $t_{2g}^3 e_g^1$. Then thermopower in the high-temperature limit is evaluated to be $S_B = -k_B \ln[5/4 \cdot x/(1-x)]/e$. Therefore, S_∞ for $x > 0.3$ is evaluated to be

$$S_\infty = S_A(1 - X) + S_B X, \quad (6)$$

which is in good agreement with the experimental values, where $X = 0.206$ for $x = 0.4$, $X = 0.644$ for $x = 0.5$, $X = 0.973$ for $x = 0.6$, and $X = 1.000$ for $x = 0.7$, respectively. This means that the JT distortion is gradually effective for polaron formation with increasing x, so that the crystal structure above room temperature changes from the orthorhombic *Pbnm* phases with $x \leqq 0.4$ to the tetragonal *I4/mcm* phases with $x \geqq 0.5$. Similar results for $La_{1-x}Ca_xMnO_3$ were reported by Palstra *et al.*[31]

The Hall coefficient R_H for the specimens of $0.1 \leqq x \leqq 0.7$ at room temperature was measured to evaluate the carrier concentration n and the Hall mobility μ under a magnetic field of 0.85 T. The experimental error of the measured R_H was 5–35% for each sample. In the calculation of carrier concentration n, the Hall scattering factor was assumed to be 1 and to obey a single carrier model. Table 3 lists the absolute value of Hall coefficient $|R_H|$, experimental error of $|R_H|$, the carrier concentration $n = 1/e|R_H|$, and the Hall mobility $\mu = |R_H|/\rho$, respectively. As summarized in Table 3, n increased with increasing Sr content for $0.1 \leqq x \leqq 0.3$, and remained constant for $0.3 \leqq x \leqq 0.7$. On the other hand, μ maintained small values for 25–350 μm^2/Vs over the whole Sr contents at room temperature.

Figure 7 shows the power factor S^2/ρ for $0.1 \leqq x \leqq 0.7$ measured in the temperature range from 80 to 1073 K. The temperature dependence of S^2/ρ of $Pr_{1-x}Sr_xMnO_3$ ($0.1 \leqq x \leqq 0.7$) calculated from the data in Fig. 4 and 6 is plotted in Fig. 7. Obviously, the specimen of $x = 0.7$ shows the largest power factor of all the samples above room temperature. On the other hand, the specimen of $x = 0.1$ shows the largest S^2/ρ in the p-type $Pr_{1-x}Sr_xMnO_3$ specimens. The power factor for $x = 0.1$ increases up to 400–500 K and then rapidly decreases, attaining a maximum value of 7×10^{-6} W/mK^2 at 468 K.

Figure 8 shows the total thermal conductivities κ, i.e., $\kappa = \kappa_L + \kappa_e$ and the lattice thermal conductivity $\kappa_L = \kappa - \kappa_e$, where the electric thermal conductivity κ_e is calculated from the data in Fig. 4 in the temperature range from 573 to 1073 K. After subtracting κ_e from total thermal conductivity using well-known the Wiedemann-Frantz law ($\kappa_e = L_0\sigma T$), therefore, κ_L is plotted by the dashed line against the temperature in Fig. 8. Here, we assumed that the Lorenz number L_0 is equal to 2.45×10^{-8} V^2/K^2. Although the value of κ_e increased with increasing temperature, the influence of κ_e on the total thermal conductivity is very small in comparison with that of κ_L. For all specimens, κ_L is more important than κ_e, and therefore, the total thermal conductivity is mainly ascribed to κ_L. As shown in Fig. 8, κ_L increased with increasing temperature for $0.1 \leqq x \leqq 0.3$, and maintained small values for 1–2 W/mK over the whole temperature range measured for $0.4 \leqq x \leqq 0.7$.

Finally, we present the estimated dimensionless figure of merit ZT as a function of temperature for $0.1 \leqq x \leqq 0.7$. As shown in Fig. 9, the ZT value increased with increasing temperature for $0.3 \leqq x \leqq 0.7$. Clearly, the n-type specimen of $x = 0.7$ shows the largest ZT of all the samples above room temperature. In particular, the largest ZT value for $x = 0.7$ is 0.085 at 1073 K. On the other hand, the specimen of $x = 0.1$
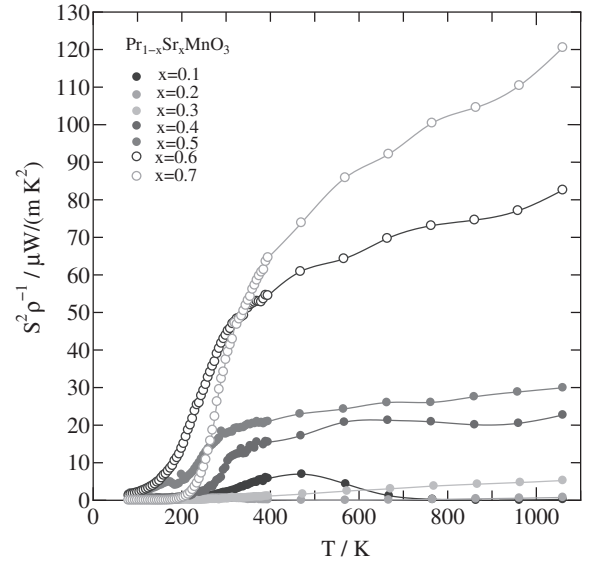

Fig. 7   Temperature (T) dependence of power factor (S^2/ρ) for $Pr_{1-x}Sr_x$-MnO$_3$ ($0.1 \leqq x \leqq 0.7$).
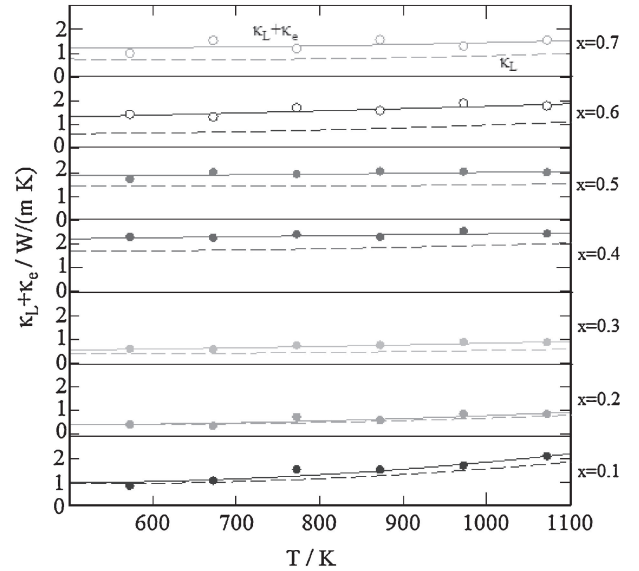

Fig. 8   The plots and solid lines show temperature (T) dependence of total thermal conductivity ($\kappa_L + \kappa_e$) above 500 K for $Pr_{1-x}Sr_xMnO_3$ ($0.1 \leqq x \leqq 0.7$). The dashed lines represent temperature (T) dependence of lattice thermal conductivity (κ_L) above 500 K for $Pr_{1-x}Sr_xMnO_3$ ($0.1 \leqq x \leqq 0.7$).

shows the largest ZT in the p-type $Pr_{1-x}Sr_xMnO_3$ specimens, attaining a maximum value of 0.0035 at 468 K.

4.   Conclusions

In this study, polycrystalline samples of $Pr_{1-x}Sr_xMnO_3$ ($0.1 \leqq x \leqq 0.7$) were synthesized using a conventional solid-state reaction method, and their crystal structures, magnetic properties and thermoelectric properties were investigated. The crystal structure at room temperature changed from orthorhombic *Pbnm* phases, with $x \leqq 0.4$, to tetragonal *I4/mcm* phases, with $x \geqq 0.5$. With increasing x, the Goldschmidt tolerance factor increases and the MnO$_6$ octahedra distortion is suppressed because of the JT distortion. The samples for $x \leqq 0.4$ show the FM like ground
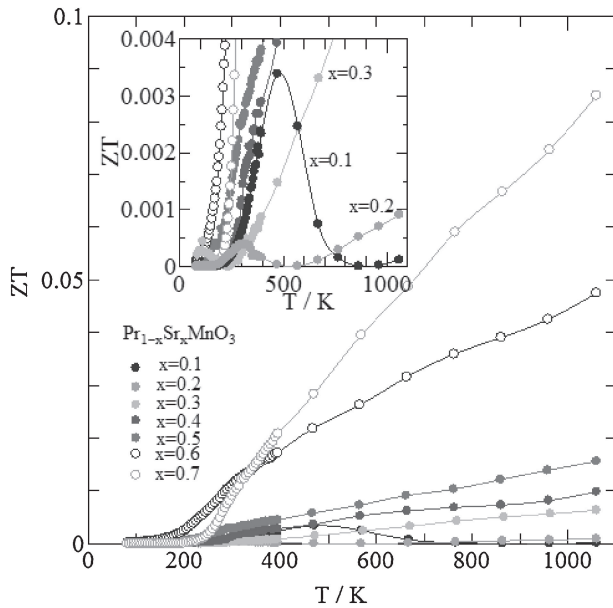
Fig. 9 Temperature (T) dependence of dimensionless figure of merit (ZT) for Pr$_{1-x}$Sr$_x$MnO$_3$ (0.1 $\leq x \leq$ 0.7). The inset also show temperature dependence of ZT, especially for $x = 0.1$, 0.2, and 0.3.

state below $T_C = 145$, 168, 271, and 310 K for $x = 0.1$, 0.2, 0.3, and 0.4, respectively. For $x = 0.5$, the ferromagnetism exists in the temperature range between $T_{CO} = 160$ K and $T_C = 310$ K. For $x > 0.5$, the ground state for $x = 0.6$ and 0.7 is the A-type AFM below $T_N = 310$ K and the C-type AFM below $T_N = 318$ K. Above room temperature, all the samples exhibit adiabatic small polaron conduction in a competition between the DE interaction and the JT distortion which is effective for the polaron formation. We found that the samples for $x = 0.1$ and 0.2 show a large positive S below room temperature and change sign from apparent holelike to electronlike behavior above 1000 K and 500 K, respectively. Thus, all the samples show a negative S at a high temperature and S_∞ defined by an extended Heikes formula is in good agreements with the experimental values for $x \geq 0.4$ by taking account of their JT distortions. We also confirmed that κ is mainly ascribed to κ_L which increases with increasing temperature for $x \leq 0.3$ and maintains constant of small value (1–2 W/mK) for $x \geq 0.4$. We obtained the largest ZT of all the samples above room temperature is 0.085 at 1073 K for $x = 0.7$. In addition, the largest ZT in the p-type specimens is obtained for $x = 0.1$, thus, attaining a maximum value of 0.0035 at 468 K. These results suggest that the potentiality to fabricate the oxide thermoelectric modules consisting of the same type of elements is valid.

Acknowledgements

REFERENCES

1) G. M. Mahan: Solid State Phys. **51** (1997) 81.
2) I. Terasaki, Y. Sasago and K. Uchinokura: Phys. Rev. B **56** (1997) R12685.
3) Y. Miyazaki, K. Kudo, M. Akoshima, Y. Ono, Y. Koike and T. Kajitani: Jpn. J. Appl. Phys. **39** (2000) L531.
4) R. Funahashi, S. Urata, K. Mizuno, T. Kouuchi and M. Mikami: Appl. Phys. Lett. **85** (2004) 1036.
5) R. Funahashi, M. Mikami, T. Mihara, S. Urata and N. Ando: J. Appl. Phys. **99** (2006) 066117.
6) S. Urata, R. Funahashi, T. Mihara, A. Kosuga, S. Sodeoka and T. Tanaka: Int. J. Appl. Ceram. Technol. **4** (2007) 535.
7) S. Ohta, H. Ohta and K. Koumoto: J. Ceram. Soc. Jpn. **114** (2006) 102.
8) M. Ohtaki, H. Koga, T. Tokunaga, K. Eguchi and H. Arai: J. Solid State Chem. **120** (1995) 105.
9) M. Iijima and N. Murayama: Proc. Int. Conf. on Thermoelectrics, (1998) p. 598.
10) K. Iwasaki, T. Ito, T. Nagasaki, Y. Arita, M. Yoshino and T. Matsui: J. Solid State Chem. **181** (2008) 3145.
11) W. Koshibae, K. Tsutsui and S. Maekawa: Phys. Rev. B **62** (2000) 6869.
12) L. Pi, C. Martin, A. Maignan and B. Raveau: Phys. Rev. B **67** (2003) 024430.
13) P. X. Thao, T. Tsuji, M. Hashida and Y. Yamamura: J. Ceram. Soc. Jpn. **111** (2003) 544.
14) B. T. Cong, T. Tsuji, P. X. Thao, P. Q. Thanh and Y. Yamamura: Physica B **352** (2004) 18.
15) G. Xu, R. Funahashi, Q. Pu, B. Liu, R. Tao, G. Wang and Z. Ding: Solid State Ionics **171** (2004) 147.
16) M. Miclau, S. Hebert, R. Retoux and C. Martin: J. Solid State Chem. **178** (2005) 1104.
17) D. Flahaut, T. Mihara, R. Funahashi, N. Nabeshima, K. Lee, H. Ohta and K. Koumoto: J. Appl. Phys. **100** (2006) 084911.
18) L. Bocher, M. H. Aguirre, D. Logvinovich, A. Shikabko, R. Robert, M. Trottmann and A. Weidenkaff: Inorg. Chem. **47** (2008) 8077.
19) R. von Helmolt, J. Wecker, B. Holzapfel, L. Schultz and K. Samwer: Phys. Rev. Lett. **71** (1993) 2331.
20) A. Urushibara, Y. Morimoto, T. Arima, A. Asamitsu, G. Kido and Y. Tokura: Phys. Rev. B **51** (1995) 14103.
21) C. Zener: Phys. Rev. **82** (1951) 403.
22) A. Maignan, C. Martin, F. Damay and B. Raveau: Phys. Rev. B **58** (1998) 2758.
23) F. Izumi and K. Momma: Solid State Phenom. **130** (2007) 15.
24) W. J. Parker, R. J. Jenkins, C. P. Butler and G. L. Abbott: J. Appl. Phys. **32** (1961) 1679.
25) Y. Tokura, Y. Tomioka, H. Kuwahara, A. Asamitsu, Y. Moritomo and M. Kasai: Physica C **263** (1996) 544.
26) Z. Jirák, J. Hejtmánek, E. Pollert, C. Martin, A. Maignan, B. Raveau, M. M. Savosta, Y. Tomioka and Y. Tokura: J. Appl. Phys. **89** (2001) 7404.
27) O. Chmaissem, B. Dabrowski, S. Kolesnik, J. Mais, J. D. Jorgensen and S. Short: Phys. Rev. B **67** (2003) 094431.
28) K. Knížek, J. Hejtmánek, Z. Jirák, C. Martin, M. Hervieu, B. Raveau, G. André and F. Bourée: Chem. Mater. **16** (2004) 1104.
29) R. D. Shannon: Acta Crystallogr. Sect. A **32** (1976) 751.
30) V. M. Goldschmidt: Natuwissenschaften **14** (1926) 477.
31) T. T. M. Palstra, A. P. Ramirez, S.-W. Cheong, B. R. Zegarski, P. Schiffer and J. Zaanen: Phys. Rev. B **56** (1997) 5104.
32) D. Emin and T. Holstein: Ann. Phys. **53** (1969) 439.
33) I. G. Austin and N. F. Mott: Adv. Phys. **18** (1969) 41.
34) L. Murawski, C. H. Chung and J. D. Mackenzie: J. Non-Crystalline Solids **32** (1979) 91.
35) R. R. Heikes and R. W. Ure: *Thermoelectricity: Science and Engineering*, (Interscience Publishers, New York-London, 1961).